

Single and Double SM-like Higgs Boson Production at Future Electron-Positron Colliders in C2HDMs

Stefania De Curtis,^{1,*} Stefano Moretti,^{2,†} Kei Yagyu,^{1,‡} and Emine Yildirim^{2,§}

¹*INFN, Sezione di Firenze, and Department of Physics and Astronomy,
University of Florence, Via G. Sansone 1, 50019 Sesto Fiorentino, Italy*

²*School of Physics and Astronomy, University of Southampton,
Southampton, SO17 1BJ, United Kingdom*

We investigate single- and double- h , the discovered Standard Model (SM)-like Higgs boson, production at future e^+e^- colliders in Composite 2-Higgs Doublet Models (C2HDMs) and Elementary 2-Higgs Doublet Models (E2HDMs) with a softly-broken Z_2 symmetry. We first survey their parameter spaces allowed by theoretical bounds from perturbative unitarity and vacuum stability as well as by future data at the Large Hadron Collider (LHC) with an integrated luminosity up to 3000 fb^{-1} under the assumption that no new Higgs boson is detected. We then discuss how different the cross sections can be between the two scenarios when κ_V , the hVV ($V = W^\pm, Z$) coupling normalised to the SM value, is taken to be the same value in the both scenarios. We find that if κ_V^2 is found to be, e.g., 0.98, then the cross sections in C2HDMs with f (the compositeness scale) in the TeV region can be maximally changed to be about -15% , -18% , -50% and -35% for the $e^+e^- \rightarrow t\bar{t}h$, $e^+e^- \rightarrow Zhh$, $e^+e^- \rightarrow e^+e^-hh$ and $e^+e^- \rightarrow t\bar{t}hh$ processes, respectively, with respect to those in E2HDMs. Thus, a future electron-positron collider has the potential to discriminate between E2HDMs and C2HDMs, even when only h event rates are measured.

*Electronic address: decurtis@fi.infn.it

†Electronic address: S.Moretti@soton.ac.uk

‡Electronic address: yagyu@fi.infn.it

§Electronic address: ey1g13@soton.ac.uk

I. INTRODUCTION

The discovered Higgs state at the LHC has properties of an isospin doublet field. Although many new physics scenarios can be embedded in such a structure, one of the simplest but important examples is a 2HDM which naturally includes a neutral Higgs state that can play the role of the discovered one. 2HDMs are furthermore well motivated theoretically [1] and generally compliant with past and present collider and other experimental data while still offering a wealth of new Higgs states.

However, 2HDMs with elementary Higgses (which we called E2HDMs) suffer, like the SM itself, from the so-called hierarchy problem. An elegant way to solve it is to presume that the discovered Higgs boson and its possible 2HDM companions are not elementary but rather composite particles to which a pseudo-Nambu-Goldstone Boson (pNGB) nature is assigned. C2HDMs embedding pNGBs arising from a new strong dynamics at the TeV scale can be constructed by explicitly imposing a specific symmetry breaking structure. Following Refs. [2, 3], we will analyse C2HDMs based on the spontaneous global symmetry breaking at a scale f , typically in the TeV region, of an $SO(6) \rightarrow SO(4) \times SO(2)$ symmetry. In these C2HDM scenarios there are five physical Higgs states just like in E2HDMs, i.e., two CP-even (h and H), one CP-odd (A) and one pair of charged (H^\pm) Higgs bosons. As intimated, we identify the (by definition) lightest h state as the discovered Higgs boson with a mass of 125 GeV. Within this construct, one can derive deviations of C2HDM couplings from those of a generic renormalisable E2HDM as well as pursue searches for new non-SM-like (composite) Higgs signals different from the elementary case. We already considered this aspect at the LHC in Ref. [3].

In this paper, we study differences in single- and double- h production cross sections at future e^+e^- colliders between E2HDMs and C2HDMs, where the latter are based on the model construction given in Refs. [2, 3]. For single- h production, there are three relevant modes: (i) Higgs-Strahlung (HS) off a Z boson via $e^+e^- \rightarrow Zh$, (ii) Vector Boson Fusion (VBF) via $e^+e^- \rightarrow e^+e^-h^1$ and (iii) associated production with top quarks via $e^+e^- \rightarrow t\bar{t}h$. The double- h production can be classified similarly by adding one more Higgs boson h to the final state, namely, we have: (i') $e^+e^- \rightarrow Zhh$, (ii') $e^+e^- \rightarrow e^+e^-hh$ and (iii') $e^+e^- \rightarrow t\bar{t}hh$.

¹ Herein, we neglect considering W^\pm induced VBF as the hW^+W^- coupling scales in all scenarios considered in the same way as hZZ .

The single- h production modes are useful to extract the hZZ coupling via (i) and (ii) plus the $ht\bar{t}$ coupling via (iii). Because of the small background cross sections typical of a future e^+e^- machine as compared to those at the LHC, one expects to measure these Higgs boson couplings with a good accuracy. For example, in Ref. [4] the 1σ error on the measurement of the hZZ and $ht\bar{t}$ couplings at the International Linear Collider (ILC) are expected to be 0.5% and 2.5%, respectively, for an energy of $\sqrt{s} = 500$ GeV and integrated luminosity of $\mathcal{L} = 500 \text{ fb}^{-1}$. Notice that, in the $e^+e^- \rightarrow t\bar{t}h$ mode, one can also have access to the AZh coupling.

The double- h production modes are naturally sensitive not only to the hZZ and $ht\bar{t}$ couplings but also to the triple Higgs boson coupling λ_{hhh} . In particular, the measurement of λ_{hhh} is quite important to reconstruct the shape of the Higgs potential, which has been known to be a very challenging task at the LHC [5, 6]. The expected precision achievable at future e^+e^- colliders in the measurement of λ_{hhh} is of $\mathcal{O}(10\%)$ [4]. This should be contrasted with the much more limited accuracy expected at the LHC, wherein λ_{hhh} can be constrained only within a factor of 3 or so [7] of the SM value. Furthermore, the heavier CP-even Higgs boson H can contribute to the double-Higgs boson production process through its propagators, thereby enabling sensitivity to the Hhh vertex, which is expected to be within a factor of 10 or so [8] in E2HDMs. In addition, the AHZ coupling becomes accessible alongside the AhZ one in associated production with top quarks. Finally, quartic couplings of the type $hhZZ$ intervene too. (Notice that AhZ and $hhZZ$ are related to the underlying gauge structure and as such are not independent couplings.) Therefore, the measurement of the aforementioned double-Higgs boson cross sections at future e^+e^- colliders is important to also extract information about additional Higgs bosons such as their masses and couplings.

We will show in this paper that there exist measurable deviations induced in C2HDMs by the dependence upon the compositeness scale in several Higgs couplings which cannot be explained in E2HDMs, no matter the choice of parameters in either scenarios. In particular, assuming a fixed value of κ_V (defined by the hVV ($V = W^\pm, Z$) coupling normalised to the SM value), the difference between predictions in the two scenarios can be even larger than 50% for the double-Higgs production processes. Hence, a future electron-positron machine has the potential to discriminate between E2HDMs and C2HDMs.

The plan of our paper is as follows. In the next section, we describe the essential features of C2HDMs that will be dealt with here, concentrating on the couplings entering the afore-

mentioned production processes. In Sec. III and Sec. IV, we tackle the e^+e^- phenomenology of single- h and double- h production modes, respectively. Finally, we conclude in Sec. V.

II. C2HDMS AND THEIR RELEVANT INTERACTION TERMS

We give a brief review of our C2HDMS. The important parameter which characterises the composite nature of Higgs states is ξ , defined by v_{SM}^2/f^2 , where v_{SM} is a Vacuum Expectation Value (VEV) related to the Fermi constant via $v_{\text{SM}} = (\sqrt{2}G_F)^{-1/2} \simeq 246$ GeV. Therefore, in the $f \rightarrow \infty$ limit (or equivalently the $\xi \rightarrow 0$ limit) all predictions in C2HDMS become the same as those in E2HDMS. In C2HDMS, v_{SM} is given by the VEV $v \equiv \sqrt{v_1^2 + v_2^2}$ as

$$v_{\text{SM}} = f \sin \frac{v}{f}. \quad (1)$$

The ratio of the two VEVs is expressed by $\tan \beta = v_2/v_1$.

The pNGB Higgses are described by a non-linear σ -model associated to the coset $SO(6)/SO(4) \times SO(2)$. Their effective low-energy Lagrangian ought to be constructed according to the Callan, Coleman, Wess and Zumino prescription, following which the scalar potential in C2HDMS is generated by loop effects. Here, as in Refs. [2, 3], we aim at studying the phenomenology of C2HDMS in a rather model independent way by assuming the same general form of this potential as in E2HDMS with a softly-broken discrete Z_2 symmetry, the latter being imposed in order to avoid Flavor Changing Neutral Currents (FCNCs) at the tree level. For the Yukawa sector, we need to assume an embedding scheme for SM fermions into $SO(6)$ multiplets to build the Lagrangian at low energy. We adopt here the same setup of [3], to which we refer the reader for further details of the model construction.

After an expansion in ξ up to $\mathcal{O}(\xi)$, we obtain the following interaction Lagrangian relevant to single- and double- h production:

$$\begin{aligned} \mathcal{L}_{\text{int}} = & g_{\phi_i V V} \phi_i V_\mu V^\mu + g_{\phi_i \phi_j V V} \phi_i \phi_j V_\mu V^\mu + g_{\phi_i \phi_j V}^\mu \phi_i \phi_j V_\mu + y_{\phi_i f f} \phi_i \bar{f} f + \tilde{y}_{\phi_i f f} \phi_i \bar{f} \gamma_5 f \\ & + y_{\phi_i \phi_j f f} \phi_i \phi_j \bar{f} f + \lambda_{\phi_i \phi_j \phi_k} \phi_i \phi_j \phi_k, \end{aligned} \quad (2)$$

where $V_\mu = W_\mu(Z_\mu)$ is a charged(neutral) massive gauge boson, $f(\bar{f})$ is a SM fermion(anti-fermion) and ϕ_i represents a (pseudo)scalar boson. Notice that the dimension five term $\phi_i \phi_j \bar{f} f$ appears in C2HDMS because of their non-linear properties. Using this notation, one obtains the (pseudo)scalar boson couplings with the gauge bosons as (hereafter, we use the

shorthand notations $s_x \equiv \sin x$ and $c_x \equiv \cos x$):

$$g_{hVV} = \left(1 - \frac{\xi}{2}\right) c_\theta g_{hVV}^{\text{SM}}, \quad g_{HVV} = -\left(1 - \frac{\xi}{2}\right) s_\theta g_{hVV}^{\text{SM}}, \quad (3)$$

$$g_{hhVV} = \left[1 - \frac{\xi}{3}(1 + 5c_\theta^2)\right] g_{hhVV}^{\text{SM}}, \quad (4)$$

$$g_{AhZ}^\mu = -i\frac{g_Z}{2}s_\theta \left[\left(1 - \frac{5}{6}\xi\right) p_h^\mu - \left(1 - \frac{\xi}{6}\right) p_A^\mu \right], \quad (5)$$

$$g_{AHZ}^\mu = -i\frac{g_Z}{2}c_\theta \left[\left(1 - \frac{5}{6}\xi\right) p_H^\mu - \left(1 - \frac{\xi}{6}\right) p_A^\mu \right], \quad (6)$$

where θ is the mixing angle² between h and H and $g_Z = g/\cos\theta_W$. For the AhZ (AHZ) coupling, p_ϕ^μ ($\phi = h, H, A$) are the incoming four-momentum.

The relevant Yukawa couplings are given by:

$$y_{htt} = \left[\left(1 - \frac{3\xi}{2}\right) c_\theta + s_\theta \cot\beta \right] y_{htt}^{\text{SM}}, \quad y_{Htt} = \left[-\left(1 - \frac{3\xi}{2}\right) s_\theta + c_\theta \cot\beta \right] y_{htt}^{\text{SM}}, \quad (7)$$

$$\tilde{y}_{Att} = \left(1 + \frac{\xi}{2}\right) \cot\beta \tilde{y}_{Gtt}^{\text{SM}}, \quad y_{hhtt} = -\frac{2\xi}{3v_{\text{SM}}} \left(2 + \frac{s_{\beta+2\theta}}{s_\beta}\right) y_{htt}^{\text{SM}}. \quad (8)$$

In the limit $\xi \rightarrow 0$, the coupling y_{hhtt} vanishes: as expected there is no tree level $hht\bar{t}$ coupling in E2HDMs. We note that the above expressions of the top Yukawa couplings are common to all the four types of Yukawa interactions (I, II, X and Y) [9], so that there is no type dependence in the cross section of the process where only h is mediated such as $e^+e^- \rightarrow Zh$ and $e^+e^- \rightarrow e^+e^-h$. If we consider processes involving the propagators of H and/or A , then the type dependence appears in these cross sections through their widths. However, we have verified that such dependence is negligible so long that $\tan\beta$ is small (say, below 5 or so), which is a condition we will assume in our analysis.

Finally, the relevant trilinear Higgs self-couplings are given by:

$$\begin{aligned} \lambda_{hhh} &= \frac{1}{4v_{\text{SM}}s_{2\beta}} \left[(s_{2\beta+3\theta} - 3s_{2\beta+\theta})m_h^2 + 4s_\theta^2s_{2\beta+\theta}M^2 \right] \\ &\quad + \frac{\xi}{12v_{\text{SM}}} \left[c_\theta m_h^2 + 2s_\theta^2M^2(c_\theta + 2s_\theta \cot 2\beta) \right], \end{aligned} \quad (9)$$

$$\begin{aligned} \lambda_{Hhh} &= \frac{s_\theta}{2v_{\text{SM}}s_{2\beta}} \left[-s_{2(\beta+\theta)}(2m_h^2 + m_H^2) + (s_{2\beta} + 3s_{2(\beta+\theta)})M^2 \right] \\ &\quad + \frac{\xi}{12v_{\text{SM}}} s_\theta \left[m_H^2 - 2m_h^2 + (1 + 3c_{2\theta} + 6\cot 2\beta s_{2\theta})M^2 \right], \end{aligned} \quad (10)$$

² In the limit $\xi \rightarrow 0$, our θ is translated in terms of $\beta - \alpha$ as in Ref. [1] by the replacement: $\theta \rightarrow \pi/2 - (\beta - \alpha)$ and $H \rightarrow -H$.

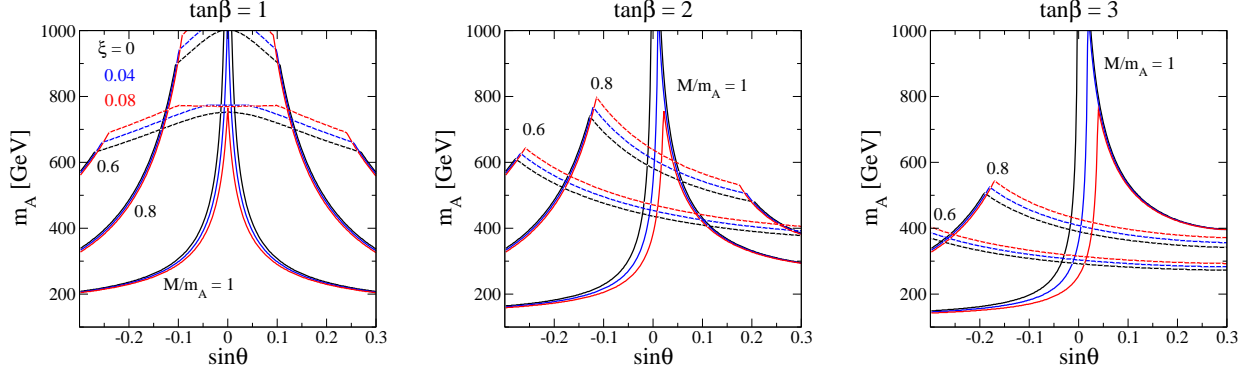


FIG. 1: Upper limit on m_A ($= m_H = m_{H^\pm}$) from unitarity (shown as the dashed part of each curve) and vacuum stability (shown as the solid part of each curve) bounds in the case of $\sqrt{s} = 1000$ GeV and $\tan\beta = 1$ (left), 2 (center) and 3 (right). The value of ξ is taken to be 0 (black), 0.04 (blue) and 0.08 (red). We also take the three different values of the ratio M/m_A (1, 0.8 and 0.6) as indicated in the figures.

where m_H and m_h are the mass of H and h , respectively, and we fix $m_h = 125$ GeV throughout the paper. We similarly define the masses of A and H^\pm by m_A and m_{H^\pm} , respectively. In Eq. (9) and (10), M describes a soft breaking scale of the Z_2 symmetry. We note that, in E2HDMs, the λ_{hhh} coupling can get $\mathcal{O}(100\%)$ corrections at the one-loop level without spoiling perturbative unitarity as it has been pointed out in Ref. [10]. They are due to non-decoupling effects of the extra Higgs boson loops, which become significant when the Higgs masses are mainly given by the Higgs VEV, i.e., the M^2 parameter is not so large as compared to the (squared) masses of the extra Higgs bosons. In our numerical analysis, we do not consider the non-decoupling case.

Before proceeding to study the discussed production modes, we ought to establish the parameter space available to C2HDMs. We first consider constraints coming from theoretical arguments, namely, perturbative unitarity and vacuum stability bounds. In Ref. [2], all the eigenvalues of the s -wave amplitude matrix for elastic scatterings of two (pseudo)scalar to two (pseudo)scalar processes have been derived up to $\mathcal{O}(s^0)$ terms in the C2HDM case. Differently from the E2HDM, there is a $s\xi$ dependence in the eigenvalues, so that we need to specify the collision energy \sqrt{s} in addition to the other parameters. For vacuum stability

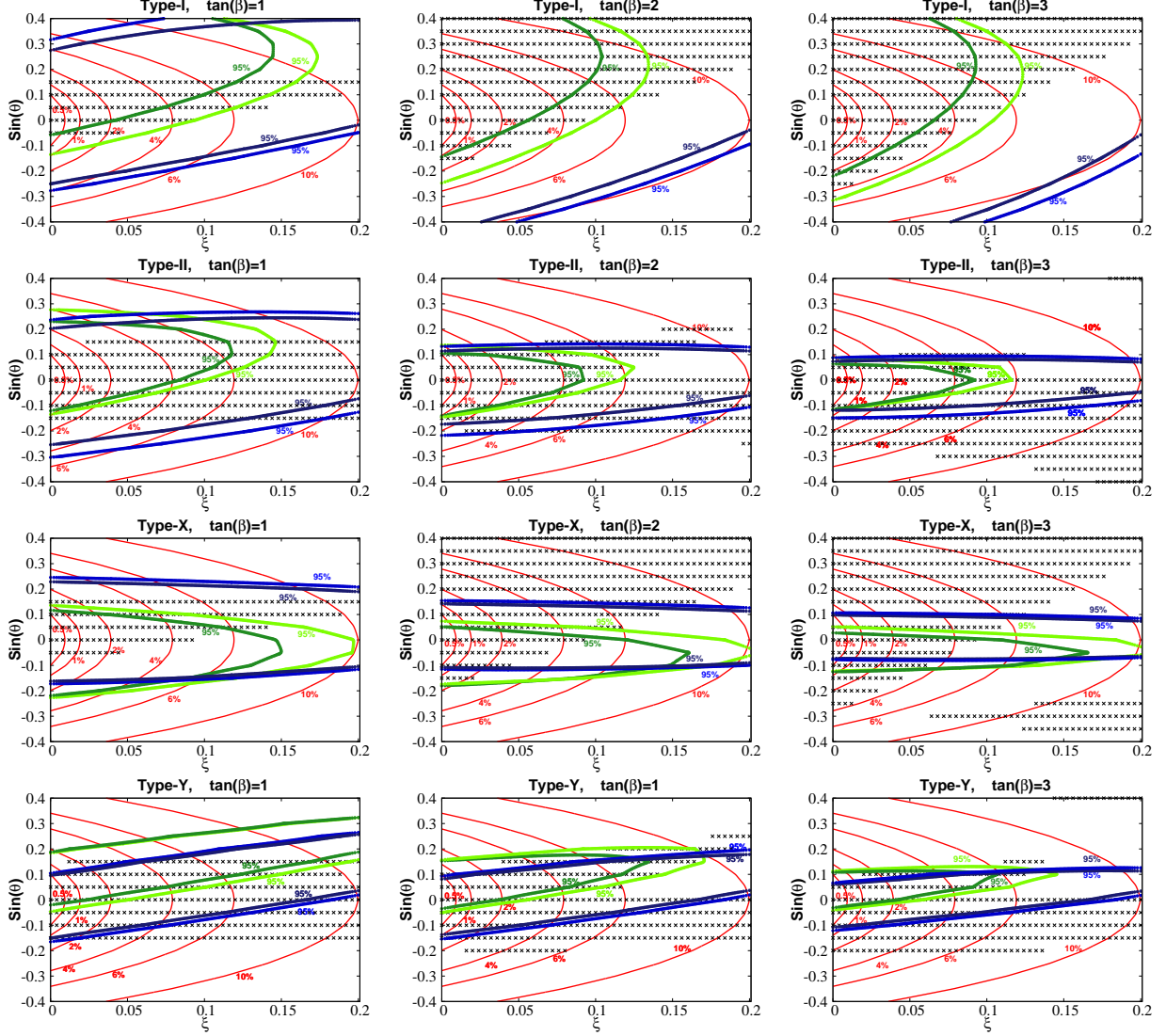


FIG. 2: Regions marked by x are allowed by the LHC data at 95% CL by using the HiggsBounds tool. The four rows show the results in the C2HDM of Type-I, Type-II, Type-X and Type-Y. The light- and dark-green (light- and dark-blue) curves display the compatibility with observed Higgs signals (SM signal strengths) at $\Delta\chi^2 = 6.18$ (95.45% CL) extrapolated to 300 fb^{-1} and 3000 fb^{-1} of luminosity respectively. Red curves are contours of $|\Delta\kappa_V| = |g_{hVV}/g_{hVV}^{\text{SM}} - 1|$. The input parameters are chosen to be $m_H = m_A = m_{H^\pm} = 500 \text{ GeV}$ and $M = 0.8m_A$. The left, center and right panels indicate $\tan\beta=1, 2$ and 3 , respectively.

bounds, we apply the same formulae given in the E2HDM [11], i.e.,

$$\lambda_1 > 0, \quad \lambda_2 > 0, \quad \sqrt{\lambda_1\lambda_2} + \lambda_3 + \min(0, \lambda_4 \pm \lambda_5) > 0. \quad (11)$$

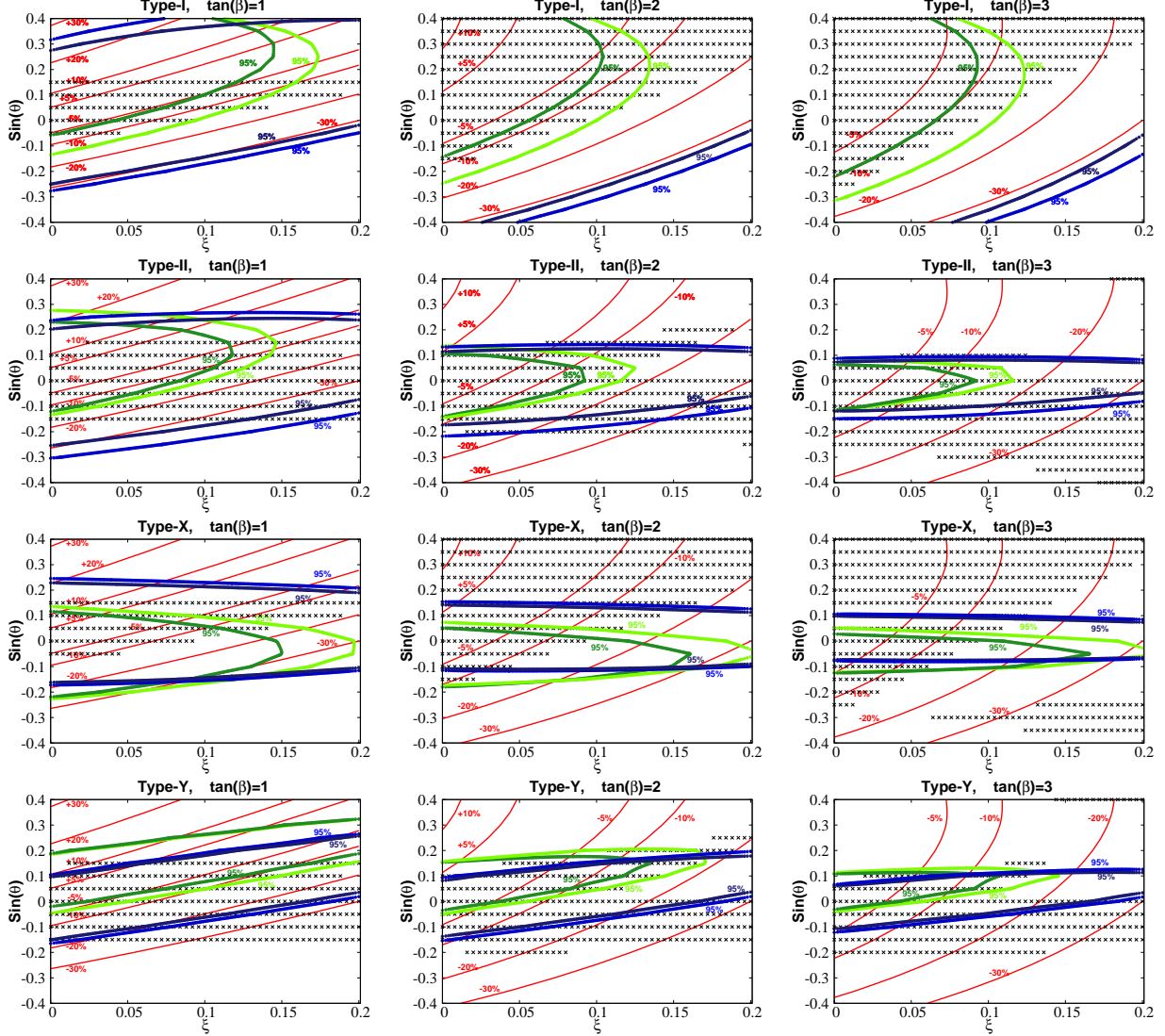


FIG. 3: Same as Fig. 2, but the red curves are contours of $\Delta\kappa_t = y_{h\bar{t}t}/y_{h\bar{t}t}^{\text{SM}} - 1$.

In Fig. 1, we show the upper limit on m_A ($= m_H = m_{H^\pm}$) as a function of $\sin\theta$ for a fixed value of $\tan\beta = 1$ (left), 2 (center) and 3 (right). The black, blue and red curves show the case for $\xi = 0, 0.04$ and 0.08 , respectively. To calculate the unitarity bound, we take $\sqrt{s} = 1000$ GeV. We can see that the allowed region strongly depends upon the choice of the ratio M/m_A , which is taken to be 1, 0.8 and 0.6. For example, when we take $m_A = 500$ GeV, $M/m_A = 0.8$ and $\xi = 0$, the allowed region of $\sin\theta$ is obtained to be $-0.20 \lesssim \sin\theta \lesssim +0.20$ (for $\tan\beta = 1$). $-0.19 \lesssim \sin\theta \lesssim +0.14$ (for $\tan\beta = 2$) and $-0.19 \lesssim \sin\theta \lesssim -0.18$ (for $\tan\beta = 3$). If we take a larger value of ξ , then the unitarity bound is slightly relaxed as compared to the case $\xi = 0$, as it was already mentioned in Ref. [2], while the vacuum

stability bound does not change significantly. We note that the case of $M \gtrsim m_A$ is highly disfavored by the vacuum stability bound, which induces us to settle on the illustrative relation $M = 0.8m_A$ ($= m_H = m_{H^\pm}$) for the remainder of the paper.

Next, we discuss the constraints from collider experiments. We consider the situation which will emerge at the end of the LHC era concerning the investigation of the already discovered 125 GeV Higgs state and that of potential additional signals from an extended Higgs sector. Herein, we assume that no additional Higgs states will have been discovered by the LHC, neither in standard luminosity conditions (i.e., after 300 fb^{-1}) nor in high luminosity ones (i.e., after 3000 fb^{-1}). Even so, we need to decide whether, after such luminosity values will have been accrued, the measurements of the couplings to SM objects of the Higgs discovered state will be as at present (with, of course, a higher precision deriving from the higher statistics) or different. In this respect, we will here consider two possible scenarios. On the one hand, we will assume that current central values of such measurements will have been confirmed. On the other hand, we will assume that SM central values will eventually have been established. We will show that, under either condition, a future e^+e^- collider will be in a position to disentangle a C2HDM from an E2HDM, through the study of single- and double- h production modes.

In Figs. 2–3 we compare the Higgs sector predictions in C2HDMs (and their E2HDM limits) with the existing exclusion bounds from the LHC experiments at 95% CL via the HiggsBounds tool (v4.3.1) [12–17] on the $(\xi, \sin\theta)$ plane. We consider the usual Yukawa Type-I, -II, -X and -Y configurations for $\tan\beta = 1, 2, 3$. Also a $\Delta\chi^2$ evaluation is made via the HiggsSignal package (v1.4.0) [18] to obtain compatibility of the projected exclusion limits from measurements of signal strengths assuming the (currently) measured central values (green), as reported in Tab. II in the Appendix from ATLAS data³, as well as the SM ones (blue), with the E2HDMs ($\xi = 0$) and C2HDMs ($\xi \neq 0$) predictions after 300 fb^{-1} (light-green and -blue curves) and 3000 fb^{-1} (dark-green and -blue curves) of LHC luminosity. Herein, the green and blue contours present the $\Delta\chi^2=6.18$ (95.45% CL) regions. To be specific, we summarise in Tab. I the bounds on $\sin\theta$ in a Type-I, -II, -X and -Y C2HDM obtained by performing a 95% CL fit using the measurements listed in Tab. II

³ We could not use CMS data in this extrapolation as the public sources that we could access did not report the statistic and systematic errors on the measurements separately.

ξ	$\tan \beta = 1$	$\tan \beta = 2$	$\tan \beta = 3$
$\xi = 0$	Type-I $-0.05 \leq s_\theta \leq 0.15$	Type-I $-0.14 \leq s_\theta \leq 0.52$	Type-I $-0.22 \leq s_\theta \leq 0.51$
	Type-II $-0.12 \leq s_\theta \leq 0.10$	Type-II $-0.14 \leq s_\theta \leq 0.10$	Type-II $-0.12 \leq s_\theta \leq 0.05$
	Type-X $-0.05 \leq s_\theta \leq 0.12$	Type-X $-0.15 \leq s_\theta \leq 0.05$	Type-X $-0.13 \leq s_\theta \leq 0.03$
	Type-Y $-0.02 \leq s_\theta \leq 0.10$	Type-Y $-0.04 \leq s_\theta \leq 0.10$	Type-Y $-0.03 \leq s_\theta \leq 0.05$
$\xi = 0.04$	Type-I $0.00 \leq s_\theta \leq 0.15$	Type-I $-0.05 \leq s_\theta \leq 0.47$	Type-I $-0.10 \leq s_\theta \leq 0.45$
	Type-II $-0.07 \leq s_\theta \leq 0.15$	Type-II $-0.10 \leq s_\theta \leq 0.09$	Type-II $-0.08 \leq s_\theta \leq 0.05$
	Type-X $-0.05 \leq s_\theta \leq 0.10$	Type-X $-0.10 \leq s_\theta \leq 0.04$	Type-X $-0.12 \leq s_\theta \leq 0.02$
	Type-Y $0.00 \leq s_\theta \leq 0.15$	Type-Y $0.00 \leq s_\theta \leq 0.15$	Type-Y $0.00 \leq s_\theta \leq 0.10$
$\xi = 0.08$	Type-I $0.06 \leq s_\theta \leq 0.15$	Type-I $0.08 \leq s_\theta \leq 0.39$	Type-I $0.08 \leq s_\theta \leq 0.34$
	Type-II $-0.01 \leq s_\theta \leq 0.15$	Type-II $-0.03 \leq s_\theta \leq 0.06$	Type-II $-0.03 \leq s_\theta \leq 0.02$
	Type-X $0.00 \leq s_\theta \leq 0.07$	Type-X $0.00 \leq s_\theta \leq 0.02$	Type-X $0.00 \leq s_\theta \leq 0.01$
	Type-Y $0.06 \leq s_\theta \leq 0.15$	Type-Y $0.05 \leq s_\theta \leq 0.15$	Type-Y $0.04 \leq s_\theta \leq 0.10$

TABLE I: Allowed values of $\sin \theta$ in a Type-I, -II, -X and -Y C2HDM with fixed values of ξ and $\tan \beta$ obtained by performing both a 95% CL fit using the measurements listed in Tab. II in the Appendix and existing data at the LHC. For the former fit, statistical errors are rescaled to an integrated luminosity of 3000 fb^{-1} . Here we take $m_H = m_A = m_{H^\pm} = 500 \text{ GeV}$ and $M = 0.8m_A$.

in the Appendix with statistical errors rescaled to an integrated luminosity of 3000 fb^{-1} . Here we consider $\xi = 0, 0.04, 0.08$ (the first one corresponding to the E2HDM limit) and $\tan \beta = 1, 2, 3$.

Typically, more parameter space with positive values of $\sin \theta$ enters the 95% CL contours of the Type-I C2HDM, compared to those of the Type-II, -X and -Y C2HDMs, for both luminosity data sets. Overall, 95% CL contours obtained under the assumption of SM central values for the Higgs signal strength measurements (blue curves) enclose larger parameter regions compared to those obtained adopting (currently) measured central values of the latter (green curves), for all Yukawa types. (The experimental channels excluding most parameter regions in Figs. 2–3 are listed in Tab. III in the Appendix.)

In Figs. 2-3 we also show (in red) the contours of κ_V and κ_t defined by $\kappa_V = g_{hVV}/g_{hVV}^{\text{SM}}$ and $\kappa_t = y_{htt}/y_{htt}^{\text{SM}}$. These red lines identify the coupling deviations possible in the relevant

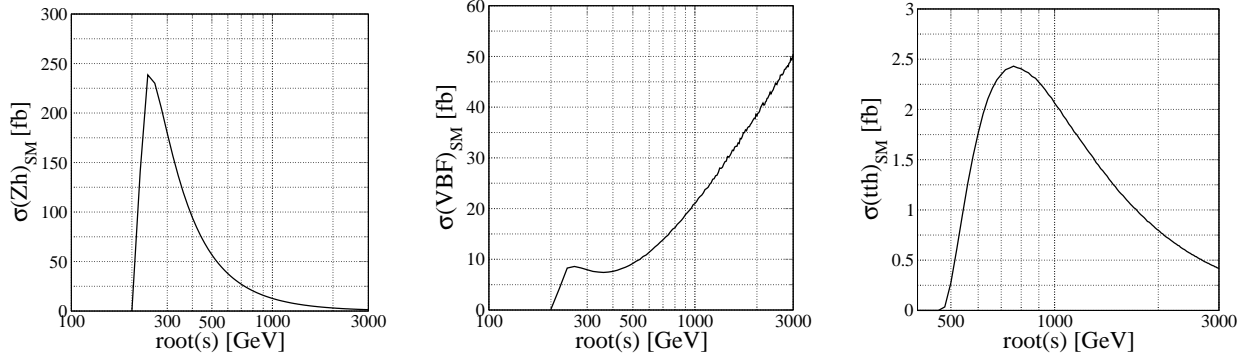


FIG. 4: Cross sections for $e^+e^- \rightarrow Zh$ (left), $e^+e^- \rightarrow e^+e^-h$ (center) and $e^+e^- \rightarrow t\bar{t}h$ (right) processes as functions of \sqrt{s} in the SM.

C2HDM (with respect to the SM) as a function of $\sin\theta$ and ξ (plus $\tan\beta$ for the Yukawa coupling) that we intend to probe using the described single- and double- h production modes, within the limits imposed by Tab. I. Note that the latter collects the most stringent bounds possible at 95% CL following the High Luminosity LHC (HL-LHC) runs (i.e., after 3000 fb^{-1} of luminosity).

III. SINGLE HIGGS BOSON PRODUCTION

In this section, we discuss the three single-Higgs boson production processes, namely, Higgs-Strahlung (HS), Vector Boson Fusion (VBF) and associated production with top quarks ($t\bar{t}h$). We calculate all the cross sections for the Type-I Yukawa interaction, but, as already stressed, for our $\tan\beta$ choices, the results are also valid for the other Yukawa types.

The reference SM cross sections for these processes are found in Fig. 4, as a function of the Centre-of-Mass (CM) energy of the collider \sqrt{s} . Here, we can see that the HS and $t\bar{t}h$ production cross sections can be maximal at just above their thresholds, i.e., $\sqrt{s} \sim 215$ and ~ 425 GeV, respectively. When \sqrt{s} gets larger, the cross sections monotonically decrease because of the s -channel topology in both cases. In contrast, for the VBF process, the cross section increases according to $\log\sqrt{s}$ due to the t -channel topology. Recall that precision on such cross sections at future e^+e^- colliders, quite irrespectively of the machine configuration and energy, is expected to be at the percent level or even less (especially for HS and VBF).

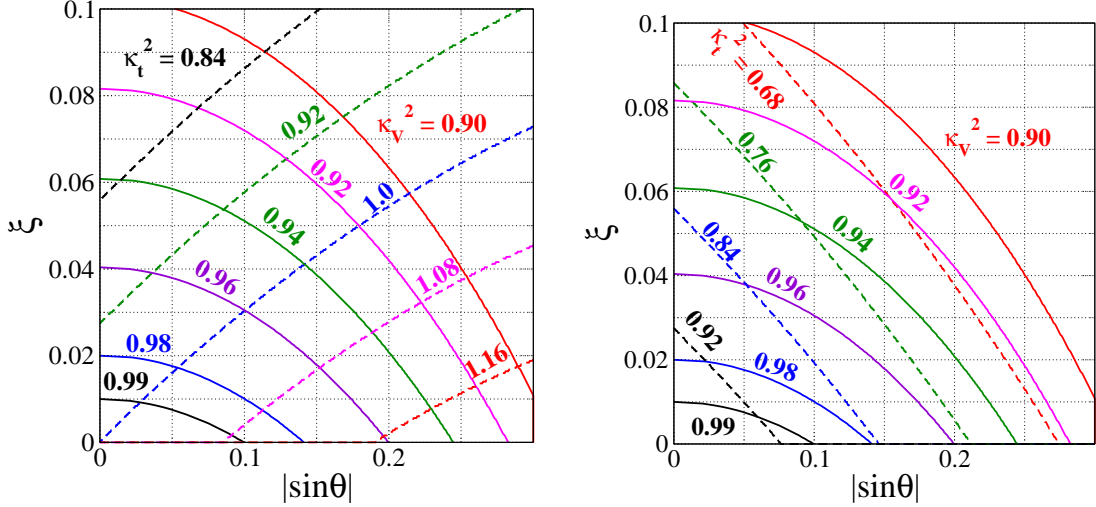


FIG. 5: Contour plots of $\kappa_V^2 = (g_{hVV}/g_{hVV}^{\text{SM}})^2$ (solid) and $\kappa_t^2 = (y_{htt}/y_{htt}^{\text{SM}})^2$ (dashed) in the $(|\sin\theta|, \xi)$ plane for $\sin\theta < 0$ (left) and $\sin\theta > 0$ (right). Contour plots of κ_t^2 are for $\tan\beta = 2$.

Let us first consider the HS and VBF processes, where, in both E2HDMs and C2HDMs, there is only one diagram containing the hZZ vertex, just like in the SM. Thus, these production cross sections are simply obtained from the corresponding ones in the SM upon multiplying for the squared scaling factor of the hZZ coupling κ_V^2 . Therefore, by measuring these cross sections, one can extract κ_V^2 .

In all C2HDM types, κ_V depends on two parameters, $|\sin\theta|$ and ξ , as we can see in Eq. (3), while in the corresponding E2HDM cases ($\xi = 0$) only one parameter is involved. This means that, if κ_V is measured at e^+e^- colliders, this determines the allowed combinations of $|\sin\theta|$ and ξ via Eq. (3). In Fig. 5, we show the contour of κ_V^2 on the $(|\sin\theta|, \xi)$ plane. For example, if $\kappa_V^2 = 0.94$ (the green solid curve), the value of $|\sin\theta|$ is determined to be about 0.245 at $\xi = 0$, which corresponds to the E2HDM case, while this can vary from 0 to 0.245 in the C2HDM one by varying ξ from about 0.06 to 0. Therefore, in order to disentangle ξ and $|\sin\theta|$ in C2HDMs, we need further inputs from experiment. In particular, once κ_V is fixed, one can then predict the deviations expected in κ_t by fixing the sign of $\sin\theta$ and the value of $\tan\beta$. This way, in fact, one can get κ_t from Eq. (7). The κ_t contours are also shown in Fig. 5. In contrast, in the E2HDM case, once κ_V and $\tan\beta$ are known, only two values of κ_t , depending on the sign of $\sin\theta$, are uniquely obtained. This delineates therefore a strategy to follow in order to possibly separate the two assumptions of 2HDMs,

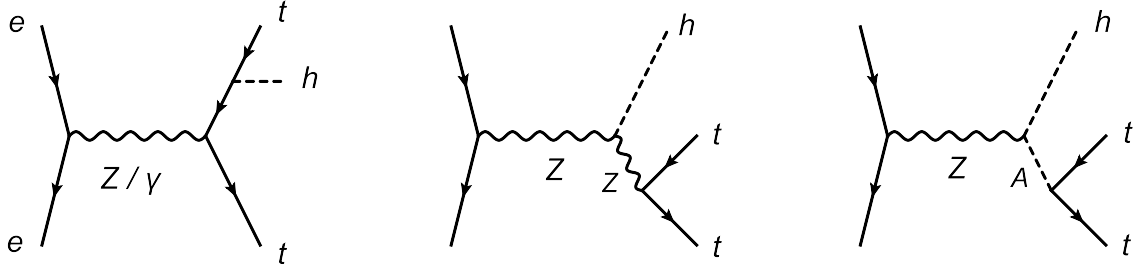


FIG. 6: Representative Feynman diagrams for the $e^+e^- \rightarrow t\bar{t}h$ process.

elementary and composite, i.e., via the simultaneous extraction of κ_V from HS and VBF and measurement of the event rates for associated production with top quarks. In short, at fixed κ_V^2 , there could well be values of the $t\bar{t}h$ cross section obtainable in C2HDMs which are instead unattainable in E2HDMs.

Before doing so though, let us investigate the $t\bar{t}h$ production cross section as a function of $\sin\theta$, ξ and $\tan\beta$. Contrary to the HS and VBF cases, this process requires a more involved treatment. As clear from Fig. 6, there are three representative diagrams entering such a process, namely: (i) $e^+e^- \rightarrow t\bar{t}$ production followed by h emission from t and \bar{t} (first diagram of Fig. 6), (ii) $e^+e^- \rightarrow Z^*h$ production followed by $Z^* \rightarrow t\bar{t}$ (second diagram of Fig. 6) and (iii) $e^+e^- \rightarrow A^{(*)}h$ production followed by $A^{(*)} \rightarrow t\bar{t}$ (third diagram of Fig. 6). By looking at the functional form of g_{hVV} and g_{AhZ} in Eq. (3) and y_{htt} and \tilde{y}_{Att} in Eq. (7), it is clear that the cross section for $e^+e^- \rightarrow t\bar{t}h$ does not scale trivially with respect to the SM in neither the E2HDM nor the C2HDM case.

In Fig. 7, we show the cross section for the $t\bar{t}h$ production process as a function of $\sin\theta$ for several fixed values of $\tan\beta$ and ξ . The collision energy \sqrt{s} is taken to be 500 (left), 1000 (center) and 2000 GeV (right). We can see that the cross section gets smaller when we take a smaller value of $\sin\theta$. In addition, when we take \sqrt{s} to be 1 TeV or 2 TeV, the on-shell production of A is realised. This significantly enhances the cross section as it is seen by comparing the case for $\sqrt{s} = 500$ and 1000 or 2000 GeV. Concerning the differences between the E2HDM and C2HDM cases, parametrised by ξ , we find that the cross section is smaller for larger values of ξ . It is also seen that the ratio of the cross section with $\xi = 0$ to that with $\xi = 0.04$ (or 0.08) for a fixed value of $\tan\beta$, $\sin\theta$ and \sqrt{s} does not depend much on the choice of $\tan\beta$, $\sin\theta$ and \sqrt{s} . The ξ dependence acts quite like an overall rescaling of the $t\bar{t}h$ cross section. Significant deviations are possible between the E2HDM and C2HDM

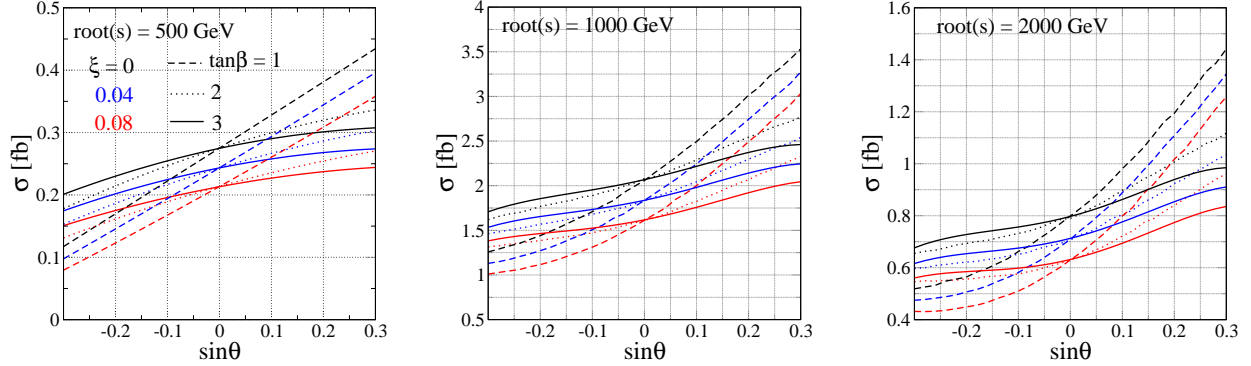


FIG. 7: Cross section for the $e^+e^- \rightarrow t\bar{t}h$ process as a function of $\sin\theta$. The value of $\tan\beta$ is taken to be 1 (dashed), 2 (dotted) and 3 (solid), and that of ξ is taken to be 0 (black), 0.04 (blue) and 0.08 (red). The collision energy and the mass of A (\sqrt{s}, m_A) is taken to be (500, 400), (1000, 500) and (2000, 500) in GeV unit for the left, center and right panels, respectively.

cases. If we compare the two scenarios for the same value of $\sin\theta$, the difference is $\mathcal{O}(20\%)$ or so in all Yukawa types, for $\sin\theta$ and ξ combinations allowed by Tab. I.

However, as intimated, what we really need to compute is the $e^+e^- \rightarrow t\bar{t}h$ cross section for a fixed value of κ_V^2 , as this will promptly be measured at future electron-positron machines via the HS and VBF processes. As stressed already, the $t\bar{t}h$ results are quite independent of the choice of the type of Yukawa interactions. In contrast, as shown in Figs. 2–3, the bounds from collider data are different for the various 2HDM types. In Tab. I we have reported the 95% CL bounds on $\sin\theta$ after 3000 fb^{-1} of LHC accumulated data, for fixed ξ and $\tan\beta$. Under the hypothesis of having measured κ_V^2 , this information determines the allowed $\sin\theta$ values that can be related to ξ , as shown in Fig. 5.

In Fig. 8, we therefore show the deviation in the $t\bar{t}h$ cross section in C2HDMs relative to E2HDMs, i.e., $\Delta\sigma \equiv (\sigma_{\text{C2HDM}}/\sigma_{\text{E2HDM}} - 1)$, as a function of ξ for two values of $\kappa_V^2 = 0.99$ and 0.98. We here take $\sqrt{s} = 1000 \text{ GeV}$, $m_A = 500 \text{ GeV}$ and $\tan\beta = 2$. Now, $|\sin\theta|$ is determined for each fixed value of ξ (see Fig. 5). Since the sign of $\sin\theta$ cannot be determined by measuring κ_V^2 , we show the cases for $\sin\theta > 0$ (solid curves) and $\sin\theta < 0$ (dashed curves) separately. The result is that we can still have a very large difference between the elementary and composite $e^+e^- \rightarrow t\bar{t}h$ cross section. For example, if the measured value of κ_V^2 were 0.98, then $\Delta\sigma$ can reach -15% for $\sin\theta > 0$. This behaviour can be explained as follows. Once κ_V^2 is specified, this fixes $|\sin\theta|$ in the E2HDM. In contrast, in the C2HDM the value

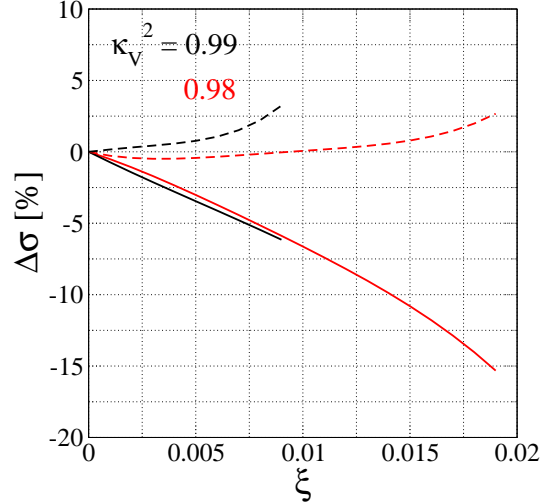


FIG. 8: Deviations in the cross section $\Delta\sigma \equiv (\sigma_{\text{C2HDM}}/\sigma_{\text{E2HDM}} - 1)$ for the $e^+e^- \rightarrow t\bar{t}h$ process at fixed $\kappa_V^2 = 0.99$ (black curves) and 0.98 (red curves). We take $\tan\beta = 2$ and $\sqrt{s} = 1000$ GeV. For each κ_V^2 , we show the case of $\sin\theta > 0$ (solid lines) and $\sin\theta < 0$ (dashed lines). We only show the result allowed by the unitarity and vacuum stability bounds and by the future LHC data assuming 3000 fb^{-1} with 95% CL. The latter bound is for the Type-I C2HDM.

of $|\sin\theta|$ can be lower depending on ξ . For the case of $\sin\theta > 0$, when the value of ξ gets large, $\sin\theta$ decreases (approaching 0). From Fig. 7, it is seen that the cross section becomes small when $\sin\theta(\xi)$ decreases(increases), so that the ratio becomes smaller. Conversely, for $\sin\theta < 0$, a larger value of ξ corresponds to a larger value of $\sin\theta$, so that the reduction of the cross section by a larger value of ξ can be cancelled through a larger value of $\sin\theta$. Either way, large values for $\Delta\sigma$, well beyond the expected precision of the $e^+e^- \rightarrow t\bar{t}h$ cross sections can be attained for allowed values of $\sin\theta$ and ξ (for a given $\tan\beta$).

In conclusion, we find that, after having enforced theoretical bounds and experimental limits from the high luminosity option of the LHC, there are parameter space regions of C2HDMs predicting cross sections for $t\bar{t}h$ production that cannot be realised in E2HDMs for a given value of $\tan\beta$ when κ_V^2 is precisely determined via the HS and VBF processes. This also suggests that we can extract the value of ξ from the measurement of the $t\bar{t}h$ yield if $\tan\beta$ is known through the study of other observables. In fact, such a parameter can be accessed at the LHC, e.g., via the precise measurement of the Yukawa couplings of the h state. In reality, one may also need to know the values of m_A , Γ_A and the $Att\bar{t}$ coupling, whenever

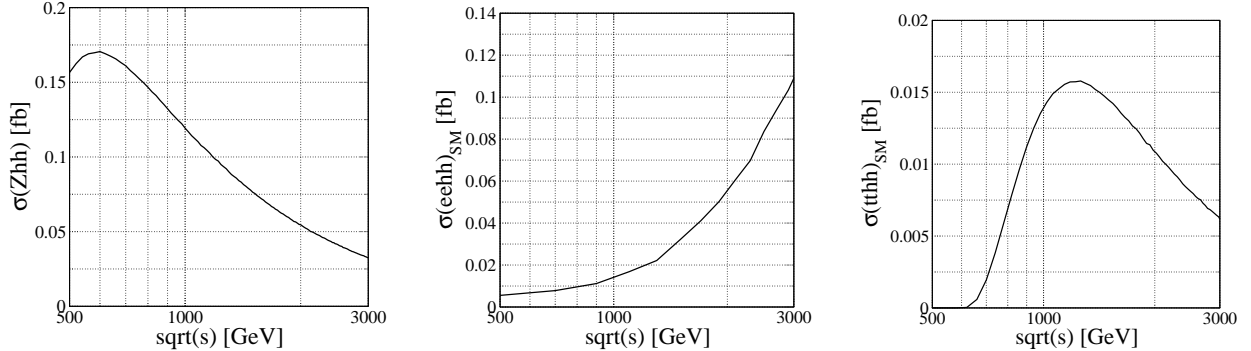


FIG. 9: Cross section of the $e^+e^- \rightarrow Zhh$ (left), $e^+e^- \rightarrow e^+e^-hh$ (center) and $e^+e^- \rightarrow t\bar{t}hh$ (right) as a function of \sqrt{s} in the SM.

the third topology in Fig. 6 contributes significantly to the $e^+e^- \rightarrow t\bar{t}h$ cross section, e.g., when it is resonant, as is the case in Fig. 7, since herein one has $m_A > 2m_t$. (Recall that the AhZ coupling is fixed by the gauge structure, which is common to both the elementary and composite Higgs scenarios we are considering, so that, unlike m_A , Γ_A and $\tilde{y}_{At\bar{t}}$, it is not an independent parameter.) As we are working under the condition (already spelt out in the introduction) that the LHC will have not produced any evidence of additional Higgs bosons other than the SM-like h state (assumption which is indeed encoded in Figs. 2–3), access to these additional parameters can be gained through the study of the $e^+e^- \rightarrow hA$ cross section and decay rates, which are promptly accessible at a future e^+e^- collider whenever $\sqrt{s} > m_h + m_A$. Ultimately, knowledge of m_A , Γ_A and the $At\bar{t}$ coupling would give access to κ_t in C2HDMs, for which large deviations from the E2HDMs counterpart are possible over allowed parameter regions, at the level of tens of percent, see red lines in Fig. 3.

IV. DOUBLE HIGGS BOSON PRODUCTION

In this section, we tackle the case of double-Higgs production, wherein the pair of final state Higgs bosons is made up by two h (SM-like) states. The production modes are those already discussed, i.e., HS ($e^+e^- \rightarrow Zhh$), VBF ($e^+e^- \rightarrow e^+e^-hh$) and associated production with top quarks ($e^+e^- \rightarrow t\bar{t}hh$). For reference, the cross sections for these processes in the SM are given in Fig. 9. Typically, in each case, the production cross section is more than hundred times smaller than the corresponding cross section for single- h production due to

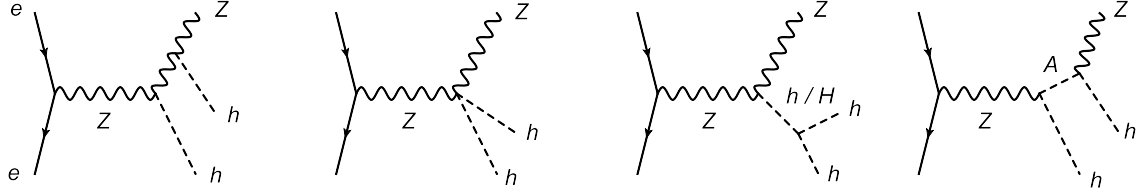


FIG. 10: Representative Feynman diagram for the $e^+e^- \rightarrow Zhh$ process.

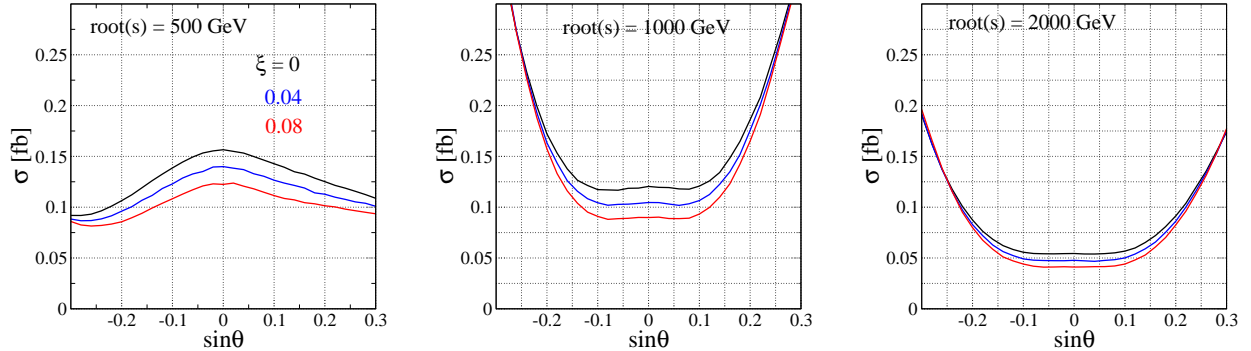


FIG. 11: Cross section for the $e^+e^- \rightarrow Zhh$ process as a function of $\sin\theta$ in the C2HDM with $\tan\beta = 2$ and $M = 0.8m_A$. The collision energy and the mass (\sqrt{s}, m_A) with $m_H = m_A$ is taken to be (500, 400), (1000, 500) and (2000, 500) in GeV unit for the left, center and right panels, respectively.

the phase space suppression. Double-Higgs production enables one to access triple-Higgs self-couplings, specifically, in the case of h pairs, the hhh and Hhh vertices. As mentioned earlier, while the constraints that can be extracted on these couplings at the LHC are rather poor, with precisions of $\mathcal{O}(100\%)$, the accuracy achievable at future e^+e^- colliders can be less close to 10%.

First of all, let us discuss the Zhh production mode. The representative Feynman diagrams are shown in Fig. 10. Differently from the single- h production case, there are here interactions depending on λ_{hhh} and λ_{Hhh} (in the third diagram), where the expressions for these couplings are given in Eqs. (9) and (10). In addition, the fourth diagram contains the propagation of A . It is important to mention here that the $\tan\beta$ dependence of the cross section for this process only enters via the λ_{hhh} and λ_{Hhh} couplings and their sensitivity to

this parameter is very weak for small θ values. In fact, for $\theta \rightarrow 0$, one has

$$\lambda_{hhh} = -\frac{m_h^2}{2v_{\text{SM}}} \left(1 - \frac{\xi}{6}\right) + \mathcal{O}(\theta^2), \quad (12)$$

$$\lambda_{Hhh} = -\frac{\theta}{2v_{\text{SM}}} \left[m_H^2 - 2m_h^2 + 4M^2 - \frac{\xi}{6}(m_H^2 - 2m_h^2 - 4M^2) \right] + \mathcal{O}(\theta^2), \quad (13)$$

wherein the $\tan\beta$ dependence only appears at the $\mathcal{O}(\theta^2)$ level.

In Fig. 11, we show the production cross section of the $e^+e^- \rightarrow Zhh$ process as a function of $\sin\theta$ for three fixed values of ξ , i.e, 0, 0.04 and 0.08. We here take $\tan\beta = 2$ (indeed, we have checked that the $\tan\beta$ dependence is essentially negligible for $|\sin\theta| \lesssim 0.2$). It is seen that the $\sin\theta$ dependence of the cross section is quite different in the case of $\sqrt{s} = 500$ GeV from those when $\sqrt{s} = 1000$ and 2000 GeV. This can be explained depending upon whether on-shell A production is possible or not. Namely, in the case of $\sqrt{s} = 500$ GeV, the diagram including A is not important, because it is off-shell, since $m_A = 400$ GeV is larger than $\sqrt{s} - m_h$. In contrast, for the cases with $\sqrt{s} = 1000$ and 2000 GeV, a non-zero value of $\sin\theta$ allows one to have on-shell production of both H and A followed by the decays $H \rightarrow hh$ and $A \rightarrow hZ$, respectively, since λ_{Hhh} and g_{AhZ} are proportional to $\sin\theta$, as seen in Eqs. (10) and (3). Therefore, at these two energies, the cross section can be enhanced due to their resonant productions. Concerning the ξ dependence, we see that deviations between the C2HDM and E2HDM case remain comparable at all energies, generally being in the 20–30% range, a result of the interplay between the fact that the aforementioned $H \rightarrow hh$ and $A \rightarrow hZ$ decays are not the dominant ones at $m_A = m_H = 500$ GeV with the ξ dependence of the HZZ and AhZ couplings.

In Fig. 12, we show the deviations in the $e^+e^- \rightarrow Zhh$ cross section from the E2HDM case appearing in the C2HDM one by considering fixed values of $\kappa_V^2 = 0.99$ and 0.98. We here take $\sqrt{s} = 1000$ GeV, $m_H = m_A = 500$ GeV, $M = 0.8m_A$ and $\tan\beta = 2$. We see that negative deviations up to about -18% seen in the case of $\kappa_V^2 = 0.98$ and $\sin\theta > 0$ are predicted also after enforcing the bounds from the high luminosity data from the LHC. The main reason for this is a decreasing $|\sin\theta|$ as ξ gets larger. As we explained above, this result is nearly independent of the choice of $\tan\beta$, so this process could be suitable to disentangle the values of ξ and $\sin\theta$ once the masses of H and A are known, e.g., from studies of the $e^+e^- \rightarrow HA$ cross section.

Next, we discuss double- h production via the VBF process. The representative Feynman diagrams are shown in Fig. 13. The HS topologies (last diagram in Fig. 13) play a sub-

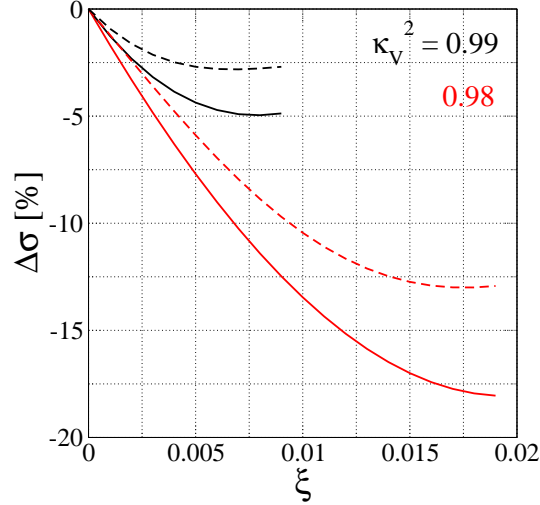


FIG. 12: Deviations in the cross section $\Delta\sigma \equiv (\sigma_{\text{C2HDM}}/\sigma_{\text{E2HDM}} - 1)$ for the $e^+e^- \rightarrow Zhh$ process at fixed $\kappa_V^2 = 0.99$ (black curves) and 0.98 (red curves). We take $\tan\beta = 2$ and $\sqrt{s} = 1000$ GeV. For each κ_V^2 , we show the case of $\sin\theta > 0$ (solid lines) and $\sin\theta < 0$ (dashed lines). We only show the result allowed by the unitarity and vacuum stability bounds and by the future LHC data assuming 3000 fb^{-1} with 95% CL. The latter bound is for the Type-I C2HDM.

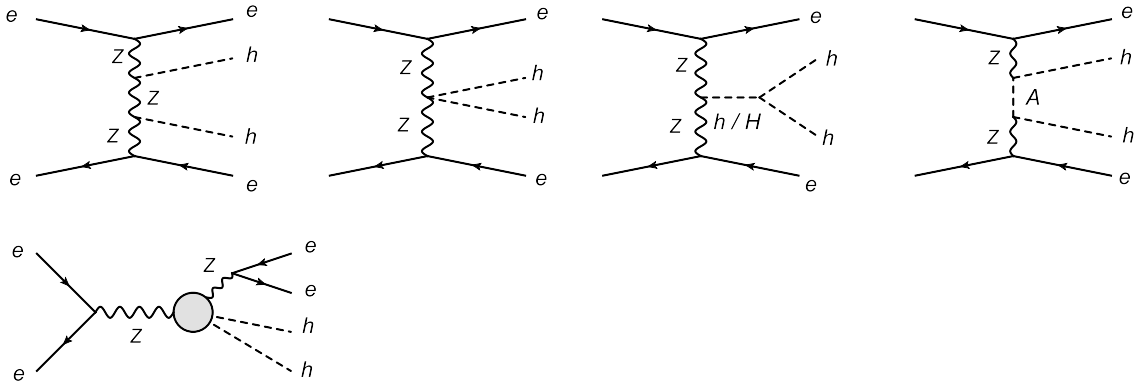


FIG. 13: Representative Feynman diagrams for the $e^+e^- \rightarrow e^+e^-hh$ process. The last diagram corresponds to the process $e^+e^- \rightarrow Zhh \rightarrow e^+e^-hh$ (see Fig. 10).

dominant role due to the tiny branching ratio of $Z \rightarrow e^+e^-$. Similarly to Zhh production, the $\tan\beta$ dependence only enters via the λ_{hhh} and λ_{Hhh} couplings, so that it is very small for small $\sin\theta$ values. The most remarkable difference with respect to Zhh production is the fact that there is no A resonance, since only the H one is possible, in the VBF process.

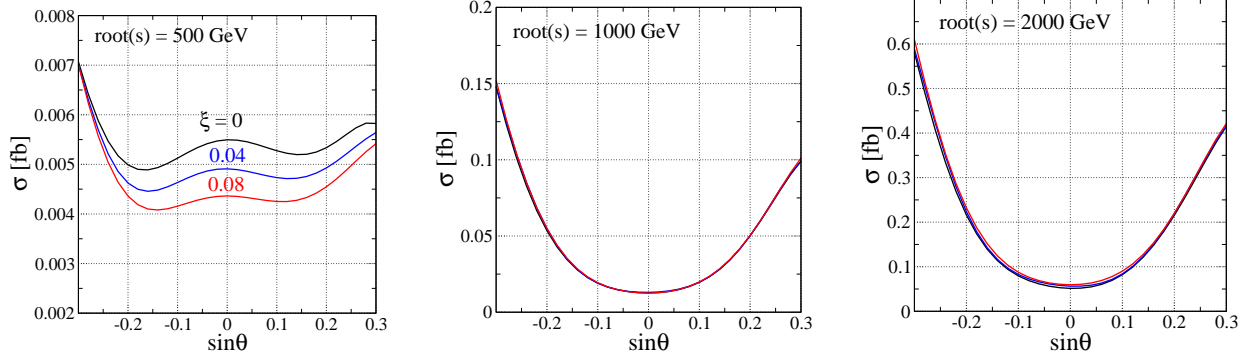


FIG. 14: Cross section of the $e^+e^- \rightarrow e^+e^-hh$ process as a function of $\sin\theta$ in the C2HDM with $\tan\beta = 2$ and $M = 0.8m_A$. The collision energy and the mass (\sqrt{s}, m_A) with $m_H = m_A$ is taken to be (500,400), (1000,500) and (2000,500) in GeV unit for the left, center and right panels, respectively.

Hence, it is not surprising to see the rather different dependence of the cross sections upon $\sin\theta$ and ξ , with respect to Fig. 11.

In Fig. 14, the cross section for the VBF process is shown as a function of $\sin\theta$ with $\tan\beta = 2$. The typical behaviour is quite similar to that seen in Zhh production. However, the difference between the C2HDM and the E2HDM evaluated for the same value of $\sin\theta$ is not so significant as compared to the Zhh case despite the absence of the A resonance.

In Fig. 15, we show the deviations in the VBF cross section as obtained in the E2HDM case relatively to the C2HDM one by taking again $\kappa_V^2 = 0.99$ and 0.98 , in line with previous examples. The behaviour is similar to that seen in Fig. 12, but the the magnitude of the deviation can be about -50% in the case of $\kappa_V^2 = 0.98$ and $\sin\theta > 0$. Here, according to Fig. 13, investigation of the hhh , Hhh and $hhZZ$ couplings would become possible in presence of the knowledge of the Zhh one (recall that the AhZ vertex is fixed by the gauge structure). Unlike the previously studied Zhh production case though, now, because the cross section of the VBF process does not significantly depend upon $\tan\beta$, one is in an excellent position to separate the values of ξ and θ .

Finally, we investigate the $t\bar{t}hh$ production process, for which the representative Feynman diagrams are shown in Fig. 16. We note (again) that the third diagram appears at the tree level only in C2HDMs, not E2HDMs, as it comes from the non-linear nature of the composite Higgs interaction. Its effect is, however, negligibly small, because the y_{hhtt} coupling given in

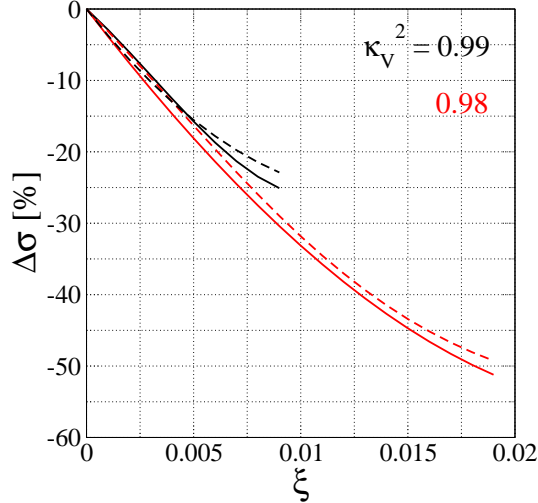


FIG. 15: Deviations in the cross section $\Delta\sigma \equiv (\sigma_{\text{C2HDM}}/\sigma_{\text{E2HDM}} - 1)$ for the $e^+e^- \rightarrow e^+e^-hh$ process at fixed $\kappa_V^2 = 0.99$ (black curves) and 0.98 (red curves). We take $\tan\beta = 2$ and $\sqrt{s} = 1000$ GeV. For each κ_V^2 , we show the case of $\sin\theta > 0$ (solid lines) and $\sin\theta < 0$ (dashed lines). We only show the result allowed by the unitarity and vacuum stability bounds and by the future LHC data assuming 3000 fb^{-1} with 95% CL. The latter bound is for the Type-I C2HDM.

Eq. (7) is proportional to ξ . Differently from the previous two double- h production modes, the $\tan\beta$ dependence is important here, i.e., it enters not only λ_{hhh} and λ_{Hhh} but also various Yukawa couplings such as y_{htt} , y_{Htt} and \tilde{y}_{Att} (other than indirectly via the Higgs widths). Therefore, this process is useful to extract independent information on $\tan\beta$ or to check its consistency with other processes if ξ , $\sin\theta$, $\tan\beta$ and the masses (plus possibly widths) of the extra Higgs bosons are known to some extent.

In Fig. 17, we show the cross section of the $t\bar{t}hh$ process as a function of $\sin\theta$ with $m_A = m_H = 500$ GeV and $M = 0.8m_A$. We take $\tan\beta = 1, 2$ and 3 for the left, center and right panels, respectively. The cross section increases when $\sin\theta \gtrsim 0$ because the $H \rightarrow hh$ decay mode opens up and diagrams with the AhZ vertex, e.g., the fourth topology in Fig. 16, become non-zero. Comparing the top ($\sqrt{s} = 1$ TeV) and bottom ($\sqrt{s} = 2$ TeV) panels we see that the cross section at $\sqrt{s} = 2$ TeV is roughly one order of magnitude larger than that at $\sqrt{s} = 1$ TeV when $\sin\theta \neq 0$. This can be explained with the opening of on-shell HA production (again, see the fourth diagram in Fig. 16) with the subsequent decays of $H \rightarrow hh$ and $A \rightarrow t\bar{t}$.

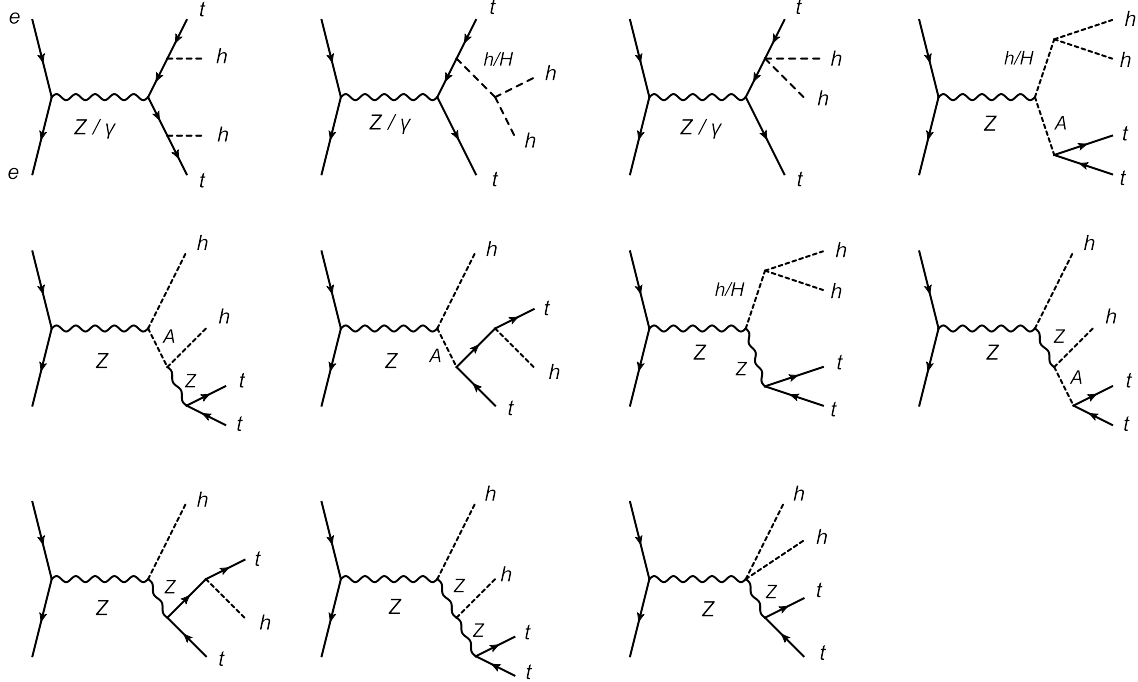


FIG. 16: Representative Feynman diagrams for the $e^+e^- \rightarrow t\bar{t}hh$ process.

Despite in both previous figures differences between the E2HDM ($\xi = 0$) and C2HDM ($\xi \neq 0$) cases can be large, up to several tens of percent in the regions allowed by Tab. I, again, differences between the two scenarios become very apparent if hVV is fixed. Thus, in Fig. 18, we show their relative cross sections of the $t\bar{t}hh$ process for a fixed value of $\kappa_V^2=0.99$ and 0.98. Here, we take $m_A = m_H = 500$ GeV, $M = 0.8m_A$, $\tan\beta = 2$ and $\sqrt{s} = 1000$ GeV. As we can see, the deviation is negative and can be more than 30% for $\kappa_V^2 = 0.98$ with positive $\sin\theta$. This is simply because of the fact that the cross section has a minimum at $\sin\theta = 0$ and there are no significant cancellations amongst the diagrams in Fig. 16. In contrast, for positive values of $\sin\theta$ the deviation can be positive, so that relative sign differences amongst the mentioned graphs can offset the generally negative rescaling of all vertices through ξ .

In short, the double- h productions can be useful to access the ξ and θ parameters by measuring the cross sections of the HS and VBF processes, since these are not simply given by the factor of κ_V^2 yet they show little sensitivity to $\tan\beta$. The $t\bar{t}hh$ production is instead useful to extract $\tan\beta$ and crucial to check the self-consistency of either Higgs scenario, elementary or composite, given the variety of particles and interactions intervening in it.

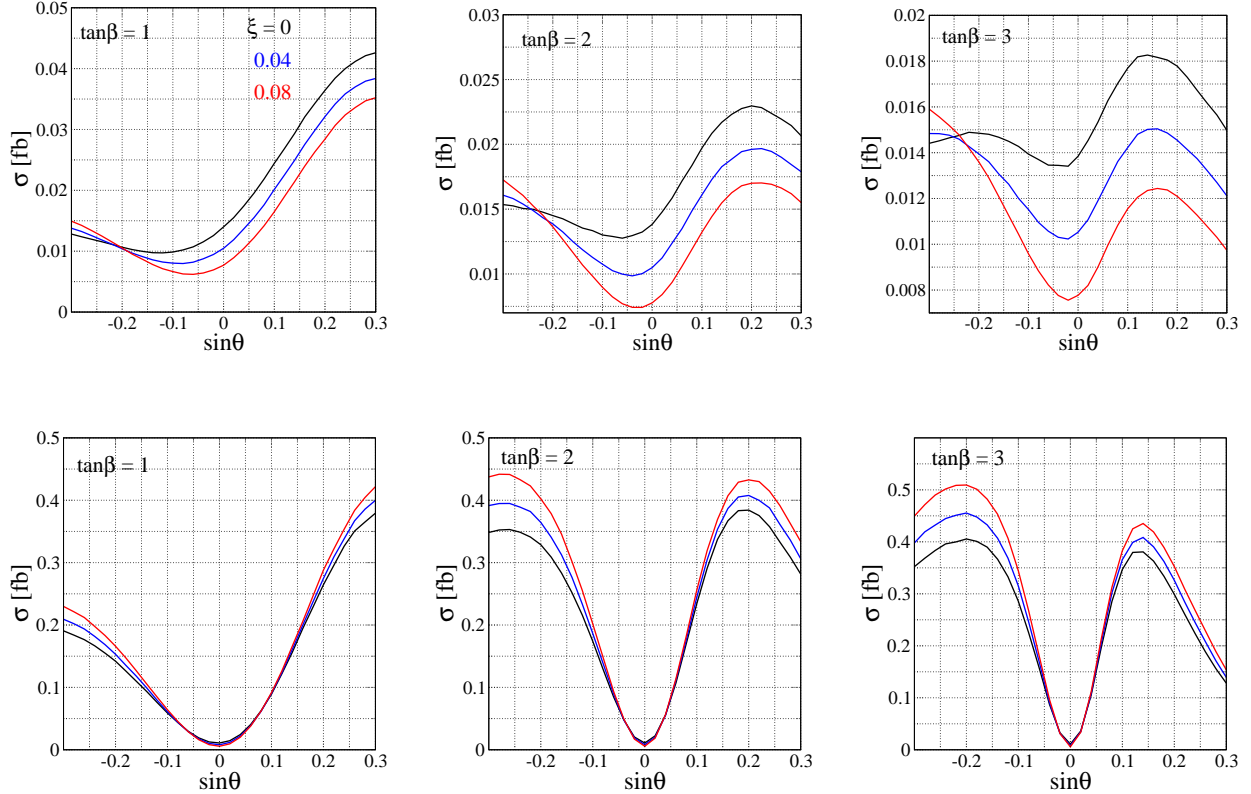


FIG. 17: Cross section of the $e^+e^- \rightarrow t\bar{t}hh$ process as a function of $\sin\theta$ in the C2HDM with $m_A = m_H = 500$ GeV and $M = 0.8m_A$. We take $\tan\beta = 1, 2$ and 3 for the left, center and right panels, respectively. The collision energy \sqrt{s} is taken to be 1000 GeV (top) and 2000 GeV (bottom).

V. CONCLUSIONS

In this study, we have continued our investigation of C2HDM scenarios, initiated by Ref. [2] and expanded in Ref. [3] (see also [19] for an overview), wherein the nature of all Higgs bosons is such that they are composite states, i.e., pNGBs from a global symmetry breaking $SO(6) \rightarrow SO(4) \times SO(2)$, induced explicitly by interactions between a new strong sector and the SM fields at a compositeness scale f . Furthermore, for the scalar potential, we assume the same general form as in the E2HDM. Within this construct, we have herein proceeded to carry out a phenomenological study aiming at establishing the potential of future e^+e^- colliders in disentangling the two hypotheses, E2HDM versus C2HDM. These machine environments afford one with a very high precision achievable in measuring the

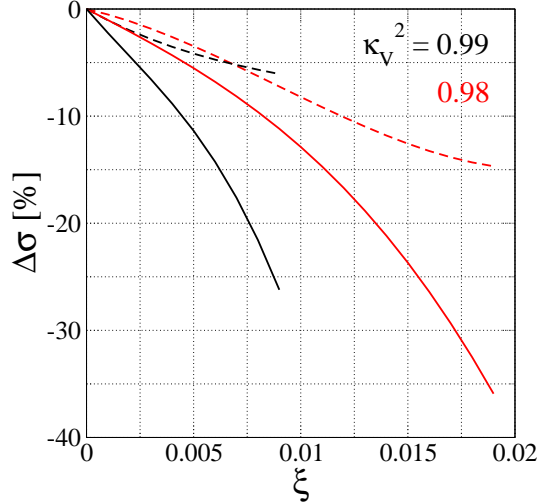


FIG. 18: Deviations in the cross section $\Delta\sigma \equiv (\sigma_{\text{C2HDM}}/\sigma_{\text{E2HDM}} - 1)$ for the $e^+e^- \rightarrow t\bar{t}hh$ process at fixed $\kappa_V^2 = 0.99$ (black curves) and 0.98 (red curves). We take $\tan\beta = 2$ and $\sqrt{s} = 1000$ GeV. For each κ_V^2 , we show the case of $\sin\theta > 0$ (solid lines) and $\sin\theta < 0$ (dashed lines). We only show the result allowed by the unitarity and vacuum stability bounds and by the future LHC data assuming 3000 fb^{-1} with 95% CL. The latter bound is for the Type-I C2HDM.

SM-like h production cross section in both single- and double- h mode, so that the rather different patterns emerging in the composite scenario with respect to the elementary one may effectively be tested. We have proven this to be the case for all available modes: i.e., HS, VBF and associated production with top quarks. Separation between the two non-minimal elementary and composite Higgs hypotheses can potentially (i.e., depending on the values of $\sin\theta$ and ξ but irrespectively of $\tan\beta$) be achieved in all channels. In fact, for some combinations of $\sin\theta$ and ξ , the C2HDM produces large, and typically negative, corrections to the SM coupling strengths, up to order -20% or so, that cannot ever be obtained in the E2HDM, thereby enabling one to promptly distinguish between the two scenarios. In other cases, when similar deviations can be obtained in both scenarios within expected accuracy for some (different in the two models) combination of inputs, one has to resort to a multi-dimensional fit assessing the CL in either hypotheses. Yet, even in this case, we expect the separation to be possible.

We have reached these conclusions assuming a Type-I setup in the Yukawa sector, although we have argued that our results are independent of the interactions of the Higgs

states with fermions, as the Yukawa dependence only enters in higher orders through the width of the heavy CP-even and CP-odd states, at least for the h production modes we have considered. Only the experimental constraints are in fact type dependent, yet the above prospects about the possibility of disentangling the two 2HDM realisations persist for all types.

This has been achieved in presence of theoretical and experimental constraints, the latter extrapolated to the end of the LHC era, assuming both a standard (up to 300 fb^{-1}) and HL (up to 3000 fb^{-1}) setup for it. We are therefore lead to conclude that future electron-positron colliders operating between 500 and 2000 GeV, of which there exist several prototypes (such as the aforementioned ILC [20–30], but also the Compact Linear Collider (CLiC) [31] and Future Circular Collider e^+e^- (FCC-ee) [32]), are the ideal testing ground to confirm or disprove the existence in Nature of either a E2HDM or C2HDM as the underlying dynamics of electro-weak symmetry breaking.

Acknowledgments

The work of SM was financed in part through the NExT Institute and by the STFC Consolidated Grant ST/J000391/1. EY was supported by the Ministry of National Education of Turkey.

Appendix

Channel	Refs.
$\tau_{\text{had}}\tau_{\text{had}}$ (VBF, 8 TeV)	[33]
$\tau_{\text{lep}}\tau_{\text{had}}$ (boosted, 8 TeV)	
$\tau_{\text{lep}}\tau_{\text{had}}$ (VBF, 8 TeV)	
$\tau_{\text{lep}}\tau_{\text{lep}}$ (boosted, 8 TeV)	
$\tau_{\text{lep}}\tau_{\text{lep}}$ (VBF, 8 TeV)	
WW (VBF enhanced, 8TeV)	[34]
ZZ (VBF, 8TeV)	[35]
multilepton	[36]
$1\ell 2\tau_{\text{had}}$ ($t\bar{t}H$, 8 TeV)	
$2\ell 0\tau_{\text{had}}$ ($t\bar{t}H$, 8 TeV)	
$2\ell 1\tau_{\text{had}}$ ($t\bar{t}H$, 8 TeV)	
3ℓ ($t\bar{t}H$, 8 TeV)	
$b\bar{b}$ (Vh, 8 TeV) with 1-lepton and 2-lepton channels	[37]
$b\bar{b}$ (Vh, 13 TeV) with 0-lepton, 1-lepton and 2-lepton channels	[38]

TABLE II: List of the Higgs data samples used in the $\Delta\chi^2$ calculations in Figs. 2–3.

Model Type	$\tan \beta = 1$	$\tan \beta = 2$	$\tan \beta = 3$
Type I	$pp \rightarrow H \rightarrow ZZ \rightarrow 4\ell$ [39] $qQ \rightarrow q'Q'h \rightarrow WW \rightarrow 2\ell 2\nu$ [42]	$pp \rightarrow H \rightarrow ZZ \rightarrow 4\ell$ [39] $qQ \rightarrow q'Q'h \rightarrow WW \rightarrow 2\ell 2\nu$ [42]	$pp \rightarrow H \rightarrow ZZ \rightarrow 4\ell$ [39] $qQ \rightarrow q'Q'h \rightarrow WW \rightarrow 2\ell 2\nu$ [42]
Type II	$pp \rightarrow H \rightarrow ZZ \rightarrow 4\ell$ [39] $qQ \rightarrow q'Q'h \rightarrow WW \rightarrow 2\ell 2\nu$ [42]	$pp \rightarrow H \rightarrow ZZ \rightarrow 4\ell$ [39] $pp \rightarrow h \rightarrow WW^* \rightarrow \ell\nu\ell\nu$ [41] $qQ \rightarrow q'Q'h \rightarrow WW \rightarrow 2\ell 2\nu$ [42] $pp \rightarrow h \rightarrow ZZ \rightarrow 4\ell$ [43]	$pp \rightarrow H \rightarrow ZZ \rightarrow 4\ell$ [39] $qQ \rightarrow q'Q'h \rightarrow WW \rightarrow 2\ell 2\nu$ [42] $pp \rightarrow h \rightarrow ZZ \rightarrow 4\ell$ [43]
Type X	$pp \rightarrow H \rightarrow ZZ \rightarrow 4\ell$ [39] $qQ \rightarrow q'Q'h \rightarrow WW \rightarrow 2\ell 2\nu$ [42]	$pp \rightarrow H \rightarrow ZZ \rightarrow 4\ell$ [39] $qQ \rightarrow q'Q'h \rightarrow WW \rightarrow 2\ell 2\nu$ [42]	$pp \rightarrow H \rightarrow ZZ \rightarrow 4\ell$ [39] $qQ \rightarrow q'Q'h \rightarrow WW \rightarrow 2\ell 2\nu$ [42]
Type Y	$pp \rightarrow H \rightarrow ZZ \rightarrow 4\ell$ [39] $qQ \rightarrow q'Q'h \rightarrow WW \rightarrow 2\ell 2\nu$ [42] $gg \rightarrow \phi(h, H) \rightarrow \tau\tau$ [44]	$pp \rightarrow H \rightarrow ZZ \rightarrow 4\ell$ [39] $pp \rightarrow H \rightarrow hh \rightarrow 4b$ [40] $pp \rightarrow H \rightarrow WW^* \rightarrow \ell\nu\ell\nu$ [41] $pp \rightarrow h \rightarrow ZZ \rightarrow 4\ell$ [43]	$pp \rightarrow H \rightarrow hh \rightarrow 4b$ [40] $qQ \rightarrow q'Q'h \rightarrow WW \rightarrow 2\ell 2\nu$ [42] $pp \rightarrow h \rightarrow ZZ \rightarrow 4\ell$ [43]

TABLE III: Higgs search channels most responsible for excluding parameter regions in Figs. 2–3.

-
- [1] G. C. Branco, P. M. Ferreira, L. Lavoura, M. N. Rebelo, M. Sher and J. P. Silva, Phys. Rept. **516**, 1 (2012), arXiv:1106.0034 [hep-ph].
- [2] S. De Curtis, S. Moretti, K. Yagyu and E. Yildirim, Phys. Rev. D **94**, 055017 (2016), arXiv:1602.06437 [hep-ph].
- [3] S. De Curtis, S. Moretti, K. Yagyu and E. Yildirim, arXiv:1610.02687 [hep-ph].
- [4] D. M. Asner *et al.*, arXiv:1310.0763 [hep-ph].
- [5] F. Gianotti *et al.*, Eur. Phys. J. **C39**, 293 (2005), arXiv:hep-ph/0204087 [hep-ph].
- [6] J. Baglio, A. Djouadi, R. Grber, M. M. Mhleitner, J. Quevillon and M. Spira, JHEP **1304**, 151 (2013), arXiv:1212.5581 [hep-ph].
- [7] See, e.g.: ATLAS Collaboration, ATL-PHYS-PUB-2016-024, ATL-PHYS-PUB-2015-046 and ATL-PHYS-PUB-2014-019.
- [8] V. Barger, L. L. Everett, C. B. Jackson, A. D. Peterson and G. Shaughnessy, Phys. Rev. D **90**, 095006 (2014), [arXiv:1408.2525 [hep-ph]].
- [9] M. Aoki, S. Kanemura, K. Tsumura and K. Yagyu, Phys. Rev. D **80**, 015017 (2009), arXiv:0902.4665 [hep-ph].

- [10] S. Kanemura, S. Kiyoura, Y. Okada, E. Senaha and C. P. Yuan, Phys. Lett. B **558**, 157 (2003), arXiv:hep-ph/0211308 [hep-ph]; S. Kanemura, Y. Okada, E. Senaha and C.-P. Yuan, Phys. Rev. D **70**, 115002 (2004), arXiv:hep-ph/0408364 [hep-ph]; S. Kanemura, M. Kikuchi and K. Yagyu, Nucl. Phys. B **896**, 80 (2015), arXiv:1502.07716 [hep-ph].
- [11] N. G. Deshpande and E. Ma, Phys. Rev. D **18**, 2574 (1978); M. Sher, Phys. Rept. **179**, 273 (1989); S. Nie and M. Sher, Phys. Lett. B **449**, 89 (1999), arXiv:hep-ph/9811234; S. Kanemura, T. Kasai and Y. Okada, Phys. Lett. B **471**, 182 (1999), [hep-ph/9903289].
- [12] P. Bechtle, O. Brein, S. Heinemeyer, G. Weiglein and K. E. Williams, Comput. Phys. Commun. **181**, 138 (2010), arXiv:0811.4169 [hep-ph].
- [13] P. Bechtle, O. Brein, S. Heinemeyer, G. Weiglein and K. E. Williams, Comput. Phys. Commun. **182**, 2605 (2011), arXiv:1102.1898 [hep-ph].
- [14] P. Bechtle *et al.* Eur. Phys. J. **C74**, 2693 (2014), arXiv:1311.0055 [hep-ph].
- [15] P. Bechtle *et al.* PoS (**CHARGED 2012**) 024 (2012), arXiv:1301.2345 [hep-ph].
- [16] P. Bechtle, S. Heinemeyer, O. Stål and T. Stefaniak, G. Weiglein, Eur. Phys. J. **C75**, 421 (2015), arXiv:1507.06706 [hep-ph].
- [17] O. Stål and T. Stefaniak, PoS (**EPS-HEP 2013**) 314, arXiv:1310.4039 [hep-ph].
- [18] P. Bechtle, S. Heinemeyer, O. Stål, T. Stefaniak and G. Weiglein, Eur. Phys. J. **C74**, 2711 (2014), arXiv:1305.1933 [hep-ph].
- [19] S. De Curtis, S. Moretti, K. Yagyu and E. Yildirim, arXiv:1612.05125 [hep-ph].
- [20] N. Phinney, ICFA Beam Dyn. Newslett. **42** (2007) 7.
- [21] G. Aarons *et al.* [ILC Collaboration], arXiv:0709.1893 [hep-ph].
- [22] N. Phinney, N. Toge and N. Walker, arXiv:0712.2361 [physics.acc-ph].
- [23] T. Behnke *et al.* [ILC Collaboration], arXiv:0712.2356 [physics.ins-det].
- [24] J. Brau *et al.* ILC-REPORT-2007-001, AAI-PUB-2007-002, BNL-79150-2007, CERN-2007-006, CHEP-A07-001, CLNS-07-1991, COCKCROFT-07-04, DESY-07-046, FERMILAB-TM-2382, JAI-2007-001, JINR-E9-2007-039, JLAB-R-2007-01, KEK-REPORT-2007-2, LBNL-62867, LNF-07-9-NT, SLAC-R-857.
- [25] J. Brau *et al.* [ILC Collaboration], arXiv:0712.1950 [physics.acc-ph].
- [26] T. Behnke *et al.* arXiv:1306.6329 [physics.ins-det].
- [27] C. Adolphsen *et al.* arXiv:1306.6328 [physics.acc-ph].
- [28] C. Adolphsen *et al.* arXiv:1306.6353 [physics.acc-ph].

- [29] T. Behnke *et al.* arXiv:1306.6327 [physics.acc-ph].
- [30] H. Baer *et al.* arXiv:1306.6352 [hep-ph].
- [31] M. Aicheler *et al.* preprint CERN-2012-007.
- [32] M. Bicer *et al.* [TLEP Design Study Working Group], JHEP **1401**, 164 (2014), arXiv:1308.6176 [hep-ex].
- [33] ATLAS Collaboration, JHEP **04**, 117 (2015), arXiv:1501.04943 [hep-ex].
- [34] ATLAS Collaboration, Phys. Rev. D **92**, 012006 (2015), arXiv:1412.2641 [hep-ex].
- [35] ATLAS Collaboration, Phys. Rev. D **91**, 012006 (2015), arXiv:1408.5191 [hep-ex].
- [36] ATLAS Collaboration, Phys. Lett. B **749**, 519 (2015), arXiv:1506.05988 [hep-ex].
- [37] ATLAS Collaboration, JHEP **01**, 069 (2015), arXiv:1409.6212 [hep-ex].
- [38] ATLAS Collaboration, ATLAS-CONF-2016-091.
- [39] ATLAS Collaboration, Eur. Phys. J. **C76**, 45 (2016), arXiv:1507.05930v2 [hep-ex].
- [40] CMS Collaboration, CMS PAS HIG-14-013.
- [41] ATLAS Collaboration, ATLAS-CONF-2012-012.
- [42] CMS Collaboration, CMS-PAS-HIG-13-022.
- [43] CMS Collaboration, CMS-PAS-HIG-13-002.
- [44] CMS Collaboration, CMS-PAS-HIG-14-029.